

Micromechanical Influence of Fabric Anisotropy and Stress Path Dependency on Liquefaction Susceptibility in Granular Soils

Published

21st July 2025

<https://doi.org/10.5802/ogeo.23>

Edited by

Ivo Herle

Institute of Geotechnical Engineering
Technische Universität Dresden
Germany

Reviewed by

Mehdi Pouragha

Civil and Environmental Engineering
Carleton University, Canada

Alejandro Martinez

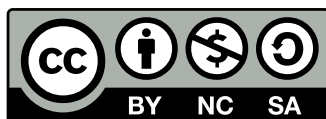
Civil and Environmental Engineering
University of California Davis, USA

Correspondence

Mohammad Salimi

Chair of Soil Mechanics, Foundation
Engineering and Environmental
Geotechnics, Ruhr-Universität Bochum,
Germany

mohammad.salimi@rub.de



This article is licensed under the Creative Commons Attribution
NonCommercial ShareAlike 4.0 License.



Open Geomechanics is member of the
Centre Mersenne for Open Scientific Publishing

Mohammad Salimi^{id a}, **Nazanin Irani**^{id a}, **Merita Tafili**^{id a}
& **Torsten Wichtmann**^{id a}

^a Chair of Soil Mechanics, Foundation Engineering and Environmental
Geotechnics, Ruhr-Universität Bochum, Germany.

Abstract. This study examines the undrained cyclic behavior of granular assemblies under true triaxial loading, with a particular focus on the micromechanical effects of initial anisotropy and Lode angle. The Discrete Element Method (DEM) is coupled with the Coupled Fluid Method (CFM) to model fluid-solid interactions under undrained conditions. Three transversely isotropic specimens, composed of elongated particles, are generated with bedding plane orientations of 0° , 45° , and 90° to represent different initial fabric conditions. Simulations are performed under constant mean total stress with a fixed Lode angle. The results reveal that both initial fabric and Lode angle significantly influence liquefaction susceptibility and shear strength. Specifically, increasing the bedding plane angle from 0° to 90° increases the number of loading cycles required to reach liquefaction, primarily due to better alignment between the bedding plane and the major principal stress direction. Furthermore, the Lode angle affects the secant shear modulus and the rate of excess pore pressure generation, underscoring its role in preliquefaction behavior.

Keywords. DEM, CFM, True triaxial, Lode angle, Fabric anisotropy.

1. Introduction

Liquefaction is recognized as one of the most catastrophic geotechnical and geological hazards, characterized by significant loss of soil strength and stiffness due to an increase in excess pore water pressure Boulanger and Seed [1995], Ishihara and Koga [1981], Rodriguez-Arriaga and Green [2018], Wichtmann et al. [2010]. This phenomenon is frequently triggered by cyclic loads such as earthquakes, traffic loads and tidal waves, leading to extensive damage to supported infrastructure Hamada [1992], Koseki et al. [1997], Rondón et al. [2009], Tokimatsu et al. [2012], Wichtmann et al. [2007], Wichtmann and Triantafyllidis [2016]. The ongoing increase in the construction of offshore structures like wind turbines, platforms, and pipelines underscores the critical importance of understanding the liquefaction potential of granular materials for these projects Ju and Mao [2024], Lin et al. [2021], Wang et al. [2020]. These structures are often built on water-saturated soils, and due to the unpredictable nature of cyclic loading from waves, wind, and earthquakes, they typically experience multidirectional forces Caous et al. [2015], Gao et al. [2022], Knittel et al. [2023]. Moreover, the direction of sediment deposition changes in various circumstances, leading to the heterogeneity of fabric Liu et al. [2013], *i.e.*, variations in the geometric arrangement and orientation of particles and voids. Nonetheless, the available laboratory data is limited to loading under axisymmetric conditions, *e.g.*, triaxial, or in particular simple shear, which may not account for the effects of anisotropic loading conditions and intermediate principal stress. Hence, only a few studies investigated the undrained cyclic behavior of sand under general stress paths (*e.g.*, Ishihara and Yasuda [1975]). Additionally, quantitative assessments of fabric require advanced photographic and radiographic techniques, such as X-ray tomography imaging Drescher and De Jong [2006], Zhao et al. [2021], which are not commonly available in standard laboratories. DEM has demonstrated its remarkable capability as a versatile tool for simulating the behavior of granular media in virtual conditions. As a result, it has been extensively utilized in engineering applications (among all, *e.g.*, González Tejada and Antolin [2022], Khabazian and Hosseininia [2020], Lashkari et al. [2019]). Owing to the peculiar ability of DEM to explore the behavior from particle scale to sample scale, a thorough analysis of granular microstructure under cyclic loading is also achievable.

The available DEM studies in the literature have primarily investigated either the effect of initial fabric, *i.e.*, the inherent anisotropy on liquefaction resistance and cyclic response or, less frequently, the impact of Lode angle on the cyclic behavior of granular soils. However, the combined effect of the initial anisotropy and the anisotropy induced by the applied stress remains mainly underexplored. For instance, Ajam Norouzi and Seyedi Hosseininia [2024] highlighted the profound effect of initial fabric on cyclic liquefaction resistance through DEM modeling under biaxial compression tests. Their results confirm that varying fabric anisotropy affects the stress paths, leading to a significant decrease in the maximum internal friction angle.

These observations align well with the triaxial undrained DEM results of Yang and Taiebat [2024], Zhang et al. [2023] where the profound dependency of cyclic liquefaction resistance of the samples on the choice of sample preparation technique and the orientation of bedding plane was reported. Focusing on microstructure evolution, Jiang et al. [2019] performed cyclic triaxial DEM tests under drained conditions and validated a stress-force-fabric relationship that analytically correlates anisotropy with shear strength. The changes in inter-particle contact fabric during the liquefaction state of sand under triaxial cyclic loading were also investigated by Zhao et al. [2024]. The study highlighted the advantages of directly tracing the path of fabric variations, providing a more intuitive representation of how induced anisotropy depends on the loading direction. In tandem with these studies, the pivotal role and induced effects of the rotation of the principal stress axis on the shear strength of granular soils under cyclic loading were also revealed by Iai et al. [2013], Mo et al. [2024]. Similarly, Wei et al. [2020] conducted a series of undrained simple shear DEM simulations under unidirectional and multidirectional loading paths. Their findings revealed that granular soils exhibit significantly different liquefaction resistance depending on the loading conditions. Specifically, compared to unidirectional loading, granular packings are more prone to liquefaction under multidirectional loading paths. As previously discussed, further investigation is needed to understand the combined effects of inherent isotropy and load-induced anisotropy on liquefaction resistance and the undrained cyclic response, which is the focus of the current study. Two primary methodologies are mainly employed in DEM simulations to model the undrained behavior of fully saturated particulate media. The constant volume method (CVM) maintains volumetric strain invariance in particulate assemblies, while the second approach couples DEM with complementary numerical methods such as computational fluid dynamics (CFD) or Smoothed-particle hydrodynamic (SPH) to incorporate pore fluid effects. To enhance the computational efficiency, Liu et al. [2015] coupled fluid methods (CFM) were developed to simulate particle-fluid interactions at the mesoscopic scale (*e.g.*, [Liu et al., 2015, Okada and Ochiai, 2007]). Significant advancements in this field include the pioneering work of Hakuno and Tarumi [1988], who integrated Darcy's law with DEM to capture pore water pressure, and subsequent developments by researchers exploring various applications from biaxial testing of ellipsoid particles to 2D saturated granular materials. Salimi and Lashkari [2020] introduced a DEM-CFM coupling scheme to model undrained responses in 3D anisotropic particulate assemblies. Multiple studies have validated the efficacy of this coupling scheme across diverse stress paths [Irani et al., 2024, Salimi et al., 2024, 2023a,b, 2025d]. Hence, the DEM-CFM coupling scheme is also employed to simulate the undrained response of particulate assemblies in this study.

The main objective of this study is to explore the influence of anisotropy in terms of initial fabric and induced by variations in applied stress on the undrained cyclic

response of granular assemblies. To achieve this, a DEM-CFM coupling scheme is used to capture the influence of fluid-solid interactions under undrained conditions. Three transversely isotropic assemblies with bedding plane angles of 0° , 45° and 90° are generated, enabling the evaluation of the effect of initial fabric, on the mechanical response of the assemblies. These samples are then sheared under general stress paths with varying Lode angles to investigate the influences of anisotropy induced by variations in applied stress. To track the evolution of the microstructure of assemblies during continuous shearing, a second-order fabric tensor based on inter-particle contact orientations is used. Additionally, variation in coordination number and redundancy index under shearing is discussed alongside the tracking of fabric evolution. The evolution of the secant shear modulus with the number of cycles is evaluated and the influence of Lode angle and initial fabric are analyzed. Lastly, the numerical description of the secant shear modulus is discussed.

2. Content flow of this study

This subsection provides an overview of the structural organization and content flow of the study. Section 3 establishes the fundamental assumptions of DEM-CFM coupling scheme, encompassing both micro and macro-scale quantities along with sample preparation methodologies. Following this, Section 4 focuses on macro-scale observations, investigating the influence of Lode angle and initial fabric on stress-strain behavior and shear modulus of the considered granular assemblies. Subsequently, Section 5 examines the evolution of microstructure by tracking fabric development and coordination number and redundancy index under continuous shearing. Finally, insights derived from microstructural analyses are employed to clarify the macro-scale observations discussed in Section 4.

3. Methodology of DEM modelling

This study uses the three-dimensional Particle Flow Code (PFC3D) Itasca [2014] to simulate the behavior of granular assemblies under undrained cyclic true triaxial loading. Given the stress-controlled nature of the applied loading and stress-strain non-coaxiality under true triaxial loading scenarios, the commonly used constant volume approach was deemed inappropriate for the purpose of this study. Hence, the DEM-CFM coupling scheme proposed by Salimi and Lashkari [2020] is employed. This method utilizes Darcy's law to simulate the behavior of particulate assemblies under specified undrained stress paths and to determine the build-up of pore water pressure. The CFM calculations have been implemented using the FISH language in PFC3D.

3.1. DEM-CFM coupling scheme

The DEM-CFM coupling scheme consists of two main components, named the solid phase and the fluid phase. The solid phase governs the behavior of the solid grains in the assembly, while the fluid phase accounts for the voids

that influence fluctuations in pore water pressure. In this study, the assemblies are fully saturated, indicating that all voids are filled with water, which represents the pore-fluid phase. To describe the solid and fluid phases, it is necessary to outline the governing equations related to the stress tensor and variations in pore water pressure increments. A detailed description of these equations is provided below.

The macro-scale stress tensor $\boldsymbol{\sigma}'$ is calculated using the outer product of micro-scale quantities as in Christoffersen et al. [1981]

$$\boldsymbol{\sigma}' = \frac{1}{V} \sum_{c=1}^{N_c} \mathbf{l}^c \otimes \mathbf{f}^c \quad (1)$$

whereby V and N_c denote the volume of the assembly and the total number of contacts, respectively. \mathbf{f}^c represents the contact force, and \mathbf{l}^c is the branch vector connecting the center of the particle to the contact point c . \otimes indicates the dyadic product of two vectors. The mean effective stress is determined as $p' = \sigma'_{ii}/3$ and deviatoric stress is calculated as $q = \sqrt{3\sigma'^*_{ij}\sigma'^*_{ij}/2}$. Here, $\sigma'^*_{ij} = \sigma'_{ij} - \delta_{ij}p'$ represents the deviatoric part of the stress tensor, whereas δ_{ij} is the identity tensor. Lode angle is defined as:

$$\cos(3\theta) = \frac{J_3}{2} \left(\frac{3}{J_2} \right)^2 \quad (2)$$

with $J_2 = \|\sigma'^*_{ij}\|$ and $J_3 = \det(\sigma'^*_{ij})$. $\det(X_{ij})$ denotes the determinant of the tensor \mathbf{X} . Deviatoric strain (ε_q) can be calculated as follows:

$$\varepsilon_q = \sqrt{\frac{2}{9} [(\varepsilon_1 - \varepsilon_2)^2 + (\varepsilon_2 - \varepsilon_3)^2 + (\varepsilon_3 - \varepsilon_1)^2]} \quad (3)$$

which ε_i ($i=1, 2$ and 3) is strain along direction i . ΔP_f denotes the pore water pressure increment within the measurement volume and is defined as follows:

$$\Delta P_f = \varepsilon_v^m E_w \quad (4)$$

wherein E_w is the bulk modulus of the fluid; and ε_v^m represents the volumetric strain of the measurement volume. The variation of pore water pressure $\Delta P'_f$ due to inflow/outflow between different measurement volumes is expressed as:

$$\Delta P'_f = \frac{E_w}{n V_m} \sum \Delta Q \quad (5)$$

whereby V_m represents the volume of the measurement domain, and n denotes the porosity. ΔQ signifies the variation in fluid volume between adjacent measurement volumes, determined using Darcy's law Salimi and Lashkari [2020]. The unbalanced force acting on particles positioned at the boundaries of the measurement volume ($F_i^{\text{unbalanced}}$) is given by:

$$F_i^{\text{unbalanced}} = (P_m + \Delta P'_f + \Delta P_f) A \quad (6)$$

P_m represents the hydrostatic pore water pressure within the measurement volume, where A represents the area on which the force is applied. The following subsection is dedicated to describing the microscale entities in this study.

3.2. Definition of micro-scale quantities

In the sense of DEM, two additional parameters are used here to explore the microstructural characteristics of assemblies: the fabric tensor, the Coordination Number (CN) and and redundancy index I_R^f . The fabric tensor can represent the packing structure and orientation of particles, contacts and voids within a soil assembly. CN shows the average number of contacts per particle.

In this study, the fabric tensor \mathbf{F} is based on inter-particle contact directions and is defined as:

$$\mathbf{F} = \frac{1}{2N_c} \sum_{k=1}^{2N_c} \mathbf{n}^k \otimes \mathbf{n}^k \quad (7)$$

In this context, \mathbf{F} describes the directional distribution of contacts. The superscript k is the k -unit contact normal vector out of $2N_c$ total contact normals, where c refers to contacts. \mathbf{n} is the unit vector perpendicular to the contact plane, *i.e.*, the contact direction. n_i^k where $i \in \{1, 2, 3\}$, stands for the direction cosine of the unit vector \mathbf{n}^k with respect to the reference axis x_i ($i=1, 2, 3$). Following the definition of fabric tensor, a scalar measure to quantify the extent of fabric anisotropy Δ is used as:

$$\Delta = \sqrt{3(\mathbf{F}^* : \mathbf{F}^*)} \quad (8)$$

\mathbf{F}^* is the deviator of the fabric tensor. $\mathbf{A} : \mathbf{B} = \text{tr}(\mathbf{A} \cdot \mathbf{B}^T) = A_{ij}B_{ij}$, with $\text{tr}(X) = X_{ii}$ as the trace of a tensor. In Eq. 8, Δ represents the intensity of anisotropy in the preferred orientation of contacts within an assembly.

The MCN and redundancy index I_R^f defined as:

$$\text{MCN} = \frac{2N_c - N_p^1}{N_p - N_p^0 - N_p^1}; \quad I_R^f = \frac{(3 - 2f_s)N_c}{6(N_p - N_p^0)} \quad (9)$$

where N_p is the total number of particles. N_p^0 denotes the count of floating particles that have no contacts. The sliding fraction, f_s , measures the percentage of slipping contacts in granular assemblies, expressed as the ratio of sliding contacts to the total active contacts.

3.3. Sample Preparation and simulation details

The specimen was modeled within a cubic space measuring $5 \times 5 \times 5 \text{ mm}^3$, enclosed with three pairs of frictionless walls. Non-spherical particles are recommended as a more realistic representation of soil assemblies compared to spherical ones Nguyen et al. [2021], Salimi et al. [2025b, 2023b], especially in order to investigate the effect of anisotropy. For this reason, three overlapping spheres, representing elongated particles with an Aspect Ratio of AR=1.8, were used as representative soil grains. Figure 1 shows the shape of these particles and the corresponding particle size distribution curve of the generated assemblies.

In general, three transversely isotropic specimens—TR0, TR45, and TR90—are generated, characterized by different initial fabrics based on bedding plane angles of 0° , 45° , and 90° , respectively. Table 2 shows a schematic representation of samples with varied initial fabric (layers of particles color-coded to show bedding plane orientation) for medium-dense samples with $p_0 = 100 \text{ kPa}$ and $e_0 = 0.589$. A

poorly graded sand, characterized by a coefficient of uniformity ($C_u = 1.5$) and a coefficient of curvature ($C_c = 1.02$), is selected due to its higher susceptibility to liquefaction compared to well-graded sands Holtz et al. [1981], Pires-Sturm and DeJong [2022]. Following the methodologies outlined in Gu et al. [2014], Guo and Zhao [2013], Yang and Wu [2017], the linear contact model was employed to represent the interactions between particles at their contact points. Due to the satisfactory performance of DEM simulations in previous works Irani et al. [2024], Salimi and Lashkari [2020], Salimi et al. [2023b], the same set of DEM parameters is used here and listed in Table 1. Nonlinear contact models, such as the Hertz-Mindlin model, can represent stress-dependent stiffness more realistically, but were not adopted in this study due to their higher computational cost and the adequate performance of the calibrated linear model in capturing the observed liquefaction phenomena. A damping ratio of 0.7 is assumed. It is important to note that the specific influence of the damping ratio is beyond the scope of this study and remains an open question for future research. Furthermore, the presented simulations do not take into account gravity effects or hydrostatic forces on inter-particle interactions.

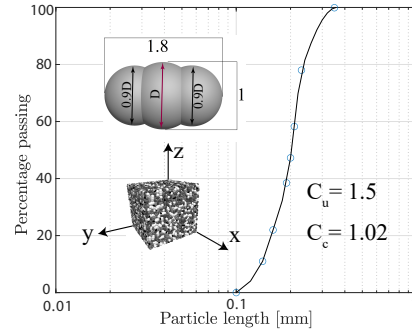


Figure 1. Particle size distribution and particle shape used in DEM modelling.

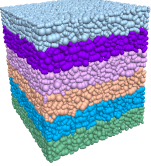
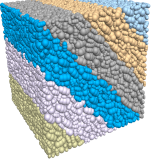
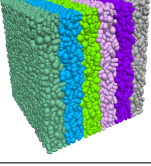
Table 1. DEM and CFM parameters

	Parameters	Value
DEM	Particle density, ρ_p	2650 (kg/m^3)
	Inter-particle friction coefficient, μ	0.5 (-)
	Damping ratio	0.7 (-)
	Wall-particle friction coefficient	0.0 (-)
	Wall stiffness	10^7 (kN/m)
	Normal contact stiffness, k_n	$k_0^\dagger r$
CFM	Tangential contact stiffness, k_s	$k_s = k_n$
	Number of clumps (pebbles)	9100 (27300)
	Bulk modulus of pore-fluid, E_w	100 (MPa)
	Pore-water density, ρ_w	1000 (kg/m^3)

$\dagger k_0 = 10^5$ (kN/m^2)

The generated particulate assemblies were initially cycled with an inter-particle friction coefficient of zero ($\mu = 0$) until reaching equilibrium. Afterward, different values of μ were applied to achieve various initial densities. The specimens were then isotropically confined at 10 kPa using a servo-control mechanism to maintain isotropic forces on the side walls, as detailed by Gu et al. [2014]. During the

Table 2. Representation of samples with varied initial fabric (layers of particles color-coded to show bedding plane orientation) for medium-dense samples with $p_0 = 100$ kPa and $e_0 = 0.589$ ($D_r \approx 0.55$).

Name	Illustration of sample deposition	Initial fabric tensor
TR0		$F_{ij} = \begin{bmatrix} 0.3031 & -0.0021 & -0.0002 \\ -0.0021 & 0.2995 & 0.0007 \\ -0.0002 & 0.0007 & 0.3973 \end{bmatrix}$
TR45		$F_{ij} = \begin{bmatrix} 0.3304 & -0.0134 & 0.0260 \\ -0.0134 & 0.3182 & -0.0230 \\ 0.0260 & -0.0230 & 0.3514 \end{bmatrix}$
TR90		$F_{ij} = \begin{bmatrix} 0.3705 & -0.0270 & 0.0023 \\ -0.0270 & 0.3143 & -0.0070 \\ 0.0023 & -0.0070 & 0.3152 \end{bmatrix}$

loading phase, μ was set to 0.5, and the total mean stress was kept constant. Micro-scale quantities were evaluated within a measurement sphere with a diameter equal to 0.9 times the larger dimension, minimizing the influence of rigid boundary constraints. The loading was applied in the z -direction by moving the boundaries at a constant velocity to impose a controlled z -axial strain. To maintain a constant mean stress and specified Lode angle during cyclic loading, a servo-controlled algorithm was employed. At each time step, the z -axial stress component was measured, and using the Lode angle definition and the constant mean stress condition, the lateral stress components in the x - and y -directions were calculated and adjusted accordingly. The pore pressure was computed using the CFM, and the corresponding effective stresses were used to control the applied boundary forces. In the post-processing stage, deviatoric stress, q , was calculated from the general formulation based on principal stress differences. While q is strictly a positive scalar by definition, we assign a negative sign to q during extension by referencing the direction of the stress path relative to the hydrostatic axis in the octahedral stress plane. This sign convention allows us to consistently distinguish between compression and extension phases, even though true tensile (negative) stresses are not present in the DEM simulation, as interparticle forces remain compressive unless cohesive models are used. Once the deviatoric stress q^{amp} reached 50 kPa during loading, the direction of loading was reversed to simulate unloading, and this process was repeated cyclically to maintain controlled stress amplitudes in both compression and extension phases. Various radial stress paths were applied, each corresponding to a fixed Lode angle, to systematically investigate the response of particulate assemblies under multidimensional stress

conditions. During each mechanical cycle, loading was imposed in the z -direction (as defined in the coordinate system shown in Figure 2) by displacing the boundaries at a constant strain rate. The inertial effects were characterized using the inertial number I , defined as [Radjai and Dubois, 2011]:

$$I = \frac{\dot{\gamma}d}{\sqrt{p/\rho}} \quad (10)$$

where $\dot{\gamma}$ is the shear strain rate, d is the particle diameter, p is the confining pressure, and ρ is the particle density. The inertial number I quantifies the ratio of inertial to confining forces, providing a measure of the dynamic regime of the granular assembly. A shear strain rate of $5 \times 10^{-5} \text{s}^{-1}$ and a time step of $1.5 \times 10^{-7} \text{s}$ were employed in the simulations. These parameters result in an inertial number of approximately 0.0003 at the onset of loading, confirming that the simulations remain within the quasi-static regime throughout the deformation process.

Changes in pore water pressure and the unbalanced forces on particles at the boundaries of the measurement volume were evaluated. The servo control mechanism in PFC3D was adjusted to maintain the specified Lode angle. This adjustment was repeated until the desired deviatoric stress amplitude (q^{amp}) was reached. Once this stress level was achieved, the loading direction was reversed. Figure 2 illustrates these proportional stress paths with constant Lode angle and indicates the sectors where stresses were applied.

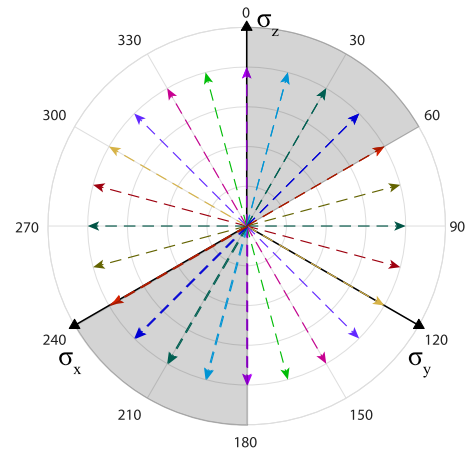


Figure 2. Proportional stress paths with a fixed Lode angle and selected sectors in this study

4. Macro-scale observations

4.1. Effect of Lode angle on the undrained cyclic response of granular assemblies

This subsection investigates the behavior of granular assemblies with the same initial fabric, stress state, and void ratio, subjected to loading paths with different values of the Lode angle. Since all samples share the same initial fabric tensor, the effect of inherent anisotropy is excluded from the subsequent analysis. Hence, only the effects of anisotropy

induced by variations in applied stress and Lode angle are analyzed. All tests are terminated once the normalized excess pore water pressure reaches $r_u = 0.99$.

To begin, only the results of DEM simulations for TR0 samples are considered. The cyclic undrained response of medium-dense TR0 samples with an initial void ratio of $e_0 = 0.589$ ($D_r \approx 0.55$) and an initial mean effective stress of $p'_0 = 100$ kPa is illustrated in Figures 3(a, d, g, j & m) and Figures 4(a, d, g, j & m). Figure 3 shows the variations of stress ratio $\eta = q/p'$ versus deviatoric strain ε_q , while Figure 4 presents the normalized excess pore water pressure r_u versus ε_q . r_u is defined as the ratio of excess pore water pressure to the initial confining pressure, i.e., $r_u = p_w/p'_0$. As illustrated in Figure 3(a), the stress ratio starts at zero and gradually increases with the strain level. When the loading mode changes to the extension regime, the stress ratio starts to decrease. Nevertheless, on both the compression and extension sides, η converges to asymptotic values of 1.4 and -1.0 , respectively. Moreover, the overall rate of changes in the stress ratio is greater in compression compared to the extension.

According to Figures 3(a, d, g, j & m), the general trend of the stress ratio evolution with deviatoric strain is qualitatively similar regardless of the Lode angle. As the principal stresses rotate with the variation of the Lode angle, it mainly affects the maximum value of η on the compression and extension sides. For instance, as the Lode angle increases from 0° to 60° in Figures 3(a and m), the maximum value of the stress ratio on the compression side decreases from 1.4 to almost 1.0, and on the extension side, it changes from -1.0 to -1.3 . It can be concluded that variations in the Lode angle affect the maximum shear strength of assemblies with the same initial state and fabric tensor. These observations are in good agreement with the results reported by Lü et al. [2017], Salimi and Lashkari [2020], where a decrease in shear strength by increasing intermediate principal stress ratio was reported for assemblies with non-spherical particles. The influence of the Lode angle is consistent along all considered bedding planes of the samples. As the Lode angle increases, the shear strength in compression decreases, while the shear strength in extension increases for all TR0, TR45 and TR90.

During the undrained tests simulated in this study, the total mean stress of $p = 100$ kPa is kept constant, while the effective mean stress p' varies due to the build-up of pore water pressure. Regarding Figure 4(a), it is observed that with each load cycle, the excess pore water pressure generally increases due to the inability of water to drain out of the sample. As pore water pressure increases, the mean effective stress decreases. A comparison between Figures 4(a, d, g, j & m) denotes the effect of the Lode angle on the generation of normalized excess pore water pressure for TR0 samples. Following a specific number of cycles, the assemblies reach a state of liquefaction, whereby the normalised excess pore water pressure, represented by the variable r_u , reaches an asymptotic value of one, resulting in a vanishing mean effective stress. In particular, all assemblies liquefy on the extension side following compression loading. While the

Lode angle affects the maximum stress ratio attained, resulting in a higher ratio in extension with increasing θ , it does not influence the mode of loading leading to liquefaction. This aligns with the observations discussed for the coordination number in Section 5.2. On the other hand, the Lode angle affects the magnitude of the strain level at which the sample liquefies, i.e., where r_u converges to 1. Moreover, θ impacts the number of cycles required to achieve the liquefaction state. In particular, for the sample sheared under $\theta = 0^\circ$, liquefaction occurs at $\varepsilon_q \approx 1.9\%$, while for $\theta = 30^\circ$, it takes place at $\varepsilon_q \approx 3.3\%$. Moreover, increasing θ from 0° to 30° impacts the rate of excess pore water pressure accumulation and decreases the number of cycles needed to reach the liquefaction state. However, further increasing the Lode angle from 30° to 45° results in an opposite trend, with $r_u = 1$ occurring at $\varepsilon_q \approx 1.9\%$. Since the number of cycles may not be clearly depicted in Figure 4, variations in shear modulus relative to the number of cycles will be examined in Sub-section 4.3. These observations underscore the influence of the Lode angle on the undrained shear strength of particulate assemblies.

4.2. Effect of initial fabric on the undrained cyclic response of granular assemblies

This subsection considers three transversely isotropic samples with different initial fabrics, while sheared with the same initial stress state, initial void ratio, and Lode angle. The focus is on investigating the effect of inherent anisotropy, i.e., the initial fabric. Figure 3 illustrates the results of the undrained true triaxial tests for medium-dense specimens with different fabrics (TR0, TR45 and TR90) sheared with $e_0 = 0.589$ ($D_r \approx 0.55$), $p'_0 = 100$ kPa. The tests were performed under two-way cyclic loading across a range of Lode angles: from 0° to 60° in the compression domain with intervals of 15° , and respectively from 180° to 240° in the extension domain. Henceforth, for brevity and clarity, only the compression domain angles will be explicitly stated, with the understanding that the corresponding extension domain angles are implicitly represented by their compression counterparts. It is noteworthy that these tests primarily elucidate the soil behavior in the pre-liquefaction state, providing crucial insights into the material's response prior to the onset of liquefaction phenomena.

A comparison between the Figures 3(a, b, & c) reveals the effect of the initial fabric on the mechanical response of samples sheared under the same initial stress state and a Lode angle of zero. The TR0 sample depicted in Figure 3(a) reaches the maximum stress ratio on the compression side at almost $\varepsilon_q \approx 1.2\%$, and on the extension side at $\varepsilon_q \approx 3.6\%$ before reaching the onset of liquefaction. However, as illustrated in Figure 3(b), changing the bedding plane angle affects the strain level at which the maximum shear strength is mobilized. In particular, for the TR45 sample, the maximum stress ratio of the compression side is reached at $\varepsilon_q \approx 1.57\%$, while in extension the sample experienced $\varepsilon_q \approx 2.5\%$ until attaining the maximum stress ratio. The role of the initial fabric on the strain level at which the maximum shear strength is achieved is also evident for other values of

θ . It is also observed that changing the bedding plane angle from 0° to 90° does not have a pronounced impact on the maximum shear strength of medium-dense assemblies.

Figures 4(a, b, & c) illustrate the effect of initial fabric on the generation of normalized excess pore water pressure of granular assemblies under undrained cyclic loading. A closer look reveals that the inclination of the bedding plane correlates with the required number of cycles to reach the liquefaction state. A comparison between Figures 4(a) and (b) indicates that changing the bedding plane angle from 0° in TR0 to 45° in TR45 results in an increase of the number of cycles in which liquefaction occurs. The same trend can be observed by further changing the bedding plane angle to 90° in TR90. For $0^\circ \leq \theta \leq 60^\circ$, the major principal stress is oriented vertically. Hence, in TR90 samples, the bedding plane is aligned parallel to the major principal stress. This alignment enables the TR90 sample to reach a liquefaction state after a higher number of cycles compared to the TR0 and TR45 samples, given the same initial state and loading conditions. These results are consistent with the DEM simulations reported by Zhang et al. [2023], where liquefaction resistance was found to be influenced by the direction of cyclic loading relative to the fabric direction. Their findings indicated that specimens with a horizontal bedding plane were more susceptible to liquefaction than those with a vertical plane under symmetrical cyclic loading conditions. The microscale observations in Section 5 will be used to further justify this behavior. It is also evident that for all Lode angle values, inherent anisotropy influences the number of cycles required to reach the liquefaction state. The following subsection illustrates the variations in shear strength with respect to the number of cycles, which will be beneficial for further discussion.

4.3. Effect of Lode angle and initial fabric on the shear modulus of undrained cyclic granular assemblies

The effect of fabric anisotropy and Lode angle on the secant shear modulus (G_{sec}) of particulate assemblies will be investigated in the following. G_{sec} is calculated as described in Figure 5 and normalized by the secant shear modulus of the first cycle, G_{sec}^1 .

Figure 6 illustrates the variation of G_{sec}^1 under different Lode angles for the TR0, TR45, and TR90 assemblies. It is evident that under $\theta = 0^\circ$, the TR90 samples exhibit the highest initial secant shear modulus, while the TR0 samples display the lowest. For TR0, an increasing trend in G_{sec}^1 is observed as the Lode angle increases, whereas TR90 shows a decreasing trend over the same range. Interestingly, TR45 initially exhibits a reduction in G_{sec}^1 up to $\theta = 30^\circ$, followed by an increasing trend toward $\theta = 60^\circ$. At $\theta = 60^\circ$, the TR0 and TR90 samples converge to similar G_{sec}^1 values. This convergence may be attributed to the fact that both assemblies are in an extension-dominated regime, where the bedding planes are approximately aligned with the major principal stress direction—resulting in comparable mechanical constraints regardless of initial anisotropy.

Following this, the analysis proceeds using normalized values ($G_{\text{sec}}/G_{\text{sec}}^1$) to facilitate a clearer comparison of stiffness degradation trends across different fabric configurations and loading paths. Normalization allows us to isolate and interpret the influence of cyclic loading and anisotropy on modulus reduction, independent of initial stiffness differences that may arise from particle alignment or fabric effects.

A comparison of $G_{\text{sec}}/G_{\text{sec}}^1$ for particulate assemblies with different initial fabrics sheared under various Lode angles is made and the results are discussed. Note that several constitutive frameworks in the literature have been developed to capture the influence of fabric and Lode angle on the mechanical behaviour of soils—among the pioneering ones are, for example, Li and Dafalias [2012], Petalas et al. [2020]. However, the present study focuses on simple correlations, which may be of interest to practitioners or serve as a basis for future constitutive model developments.

The variation of the normalized secant shear modulus G_{sec} for medium-dense TR0, TR45, and TR90 assemblies subjected to shearing within the range $0^\circ \leq \theta \leq 60^\circ$ is presented in Figure 7 with circular markers. According to Figures 7(a–e), the TR0 and TR45 assemblies exhibit comparable stiffness responses under various Lode angles, particularly for $\theta = 45^\circ \rightarrow 225^\circ$, up to approximately the 50th cycle.

Overall, the TR0 assemblies display the highest rate of stiffness degradation under cyclic loading, followed by TR45, while TR90 consistently exhibits the lowest degradation rate across all considered Lode angles. A comparison of Figure 7(a) with Figures 7(b–e) reveals that the smallest reduction in normalized G_{sec} occurs for $\theta = 0^\circ \rightarrow 180^\circ$, indicating enhanced resistance to cyclic degradation and a delayed onset of modulus collapse. In contrast, differences among the remaining Lode angles are relatively minor (cf. Figures 7(b–e)). In this sense, the highest stiffness is seen at a Lode angle of 0° . Analyzing the variation of normalized G_{sec} for the TR45 sample (cf. Figures 7(a–e)) reveals that the highest stiffness occurs at a Lode angle of 60° , while the lowest stiffness is observed at a Lode angle of 30° . Comparing the variation of normalized G_{sec} with the evolution of r_u in Figure 4 reveals a direct relationship between the generation of excess pore water pressure and the decrease in granular assembly stiffness. An increase in pore water pressure under constant volume conditions can lead to a reduction in G_{sec} , which, in turn, may accelerate strain accumulation. It is also evident that samples with bedding planes parallel to the major principal applied stress exhibit higher stiffness under identical strain levels and loading conditions. Moreover, these samples require more cycles to reduce normalized stiffness to its minimum value, which occurs during soil liquefaction.

In Figures 8–10, the relationship between the normalized secant shear modulus $G_{\text{sec}}/G_{\text{sec}}^1$ and the accumulated deviatoric strain $\varepsilon_q^{\text{acc}}$ is depicted for various test samples, specifically TR0, TR45, and TR90. The observed trends highlight the influence of multiaxial loading conditions on the degradation behavior of the shear modulus.

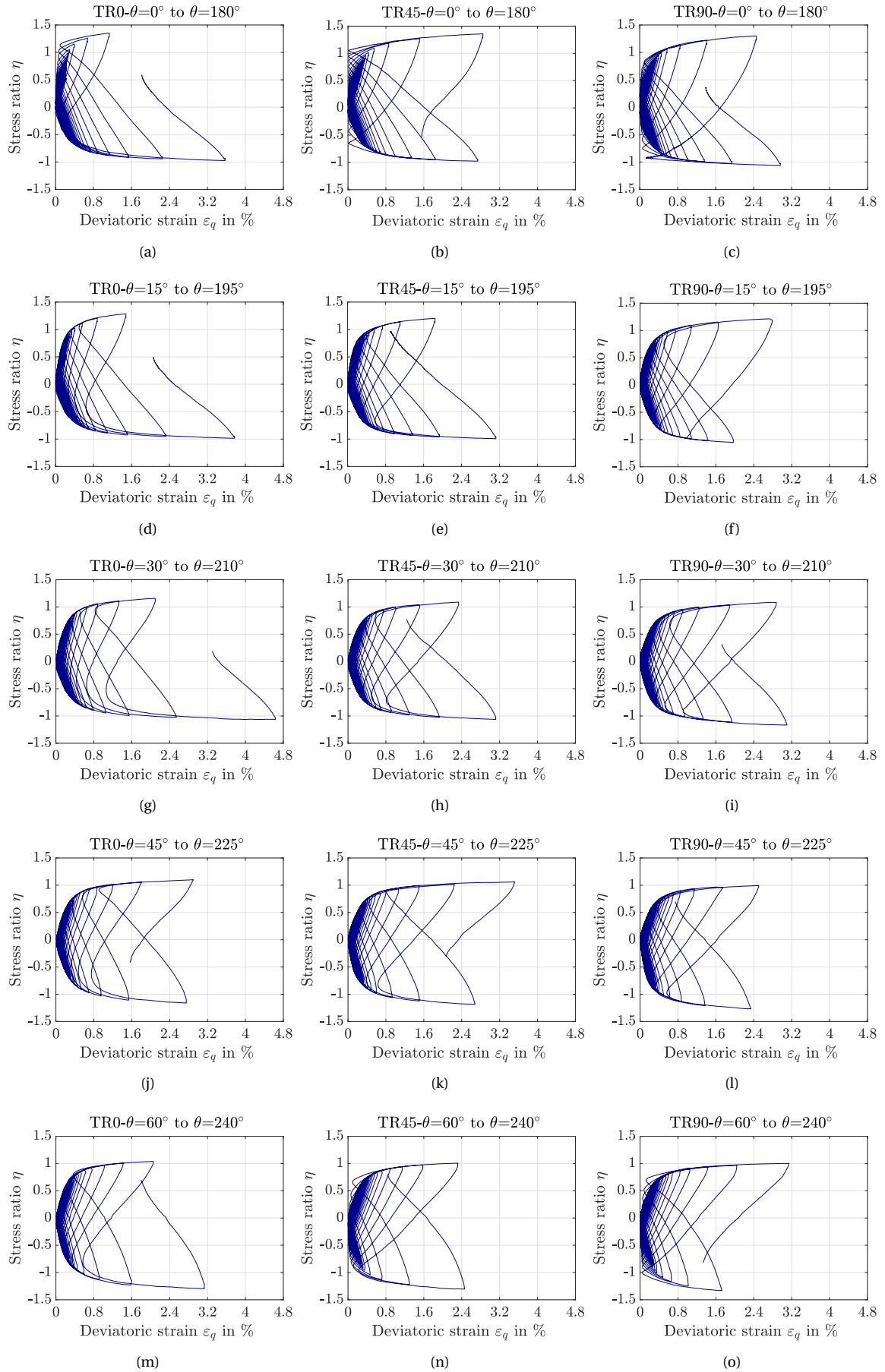


Figure 3. Mechanical response of medium-dense assemblies with $e_0 = 0.589$, $p'_0 = 100$ kPa sheared under undrained true triaxial condition in η - ε_q plane for (a, d, g, j & m): TR0, (b, e, h, k & n): TR45 and (c, f, i, l & o): TR90

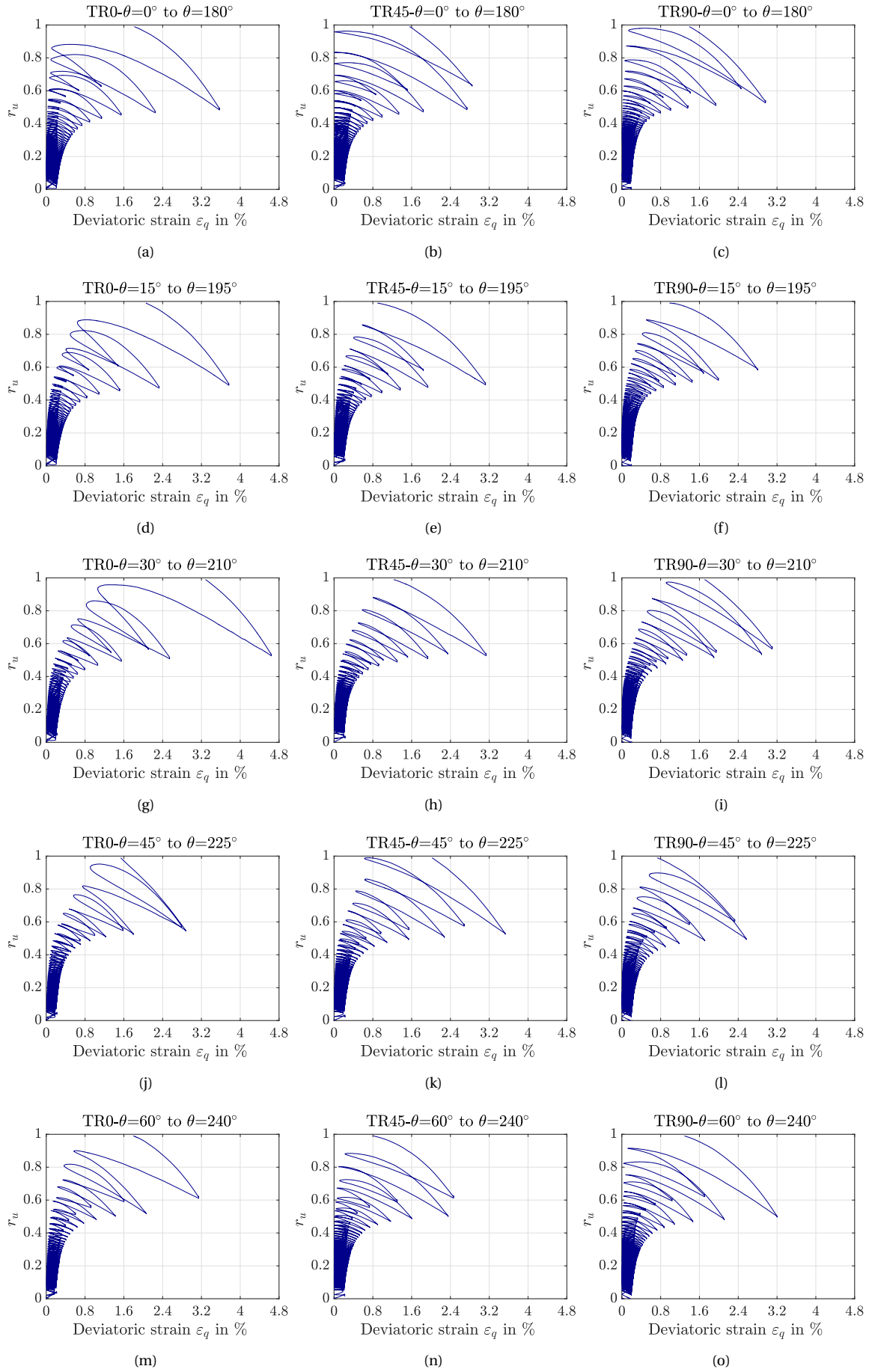


Figure 4. Mechanical response of medium-dense assemblies with $e_0 = 0.589$, $p'_0 = 100$ kPa sheared under undrained true triaxial condition in r_u - ε_q plane (a, d, g, j & m): TR0 (b, e, h, k & n): TR45 and (c, f, i, l & o): TR90

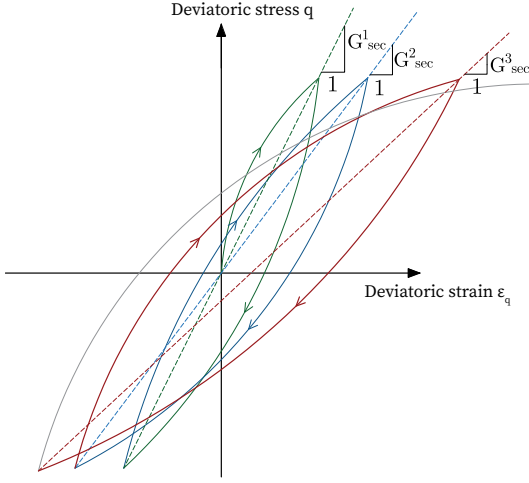


Figure 5. Sketch of the idealized shear stress-strain response of particulate assemblies alongside the methodology used to determine the shear modulus.

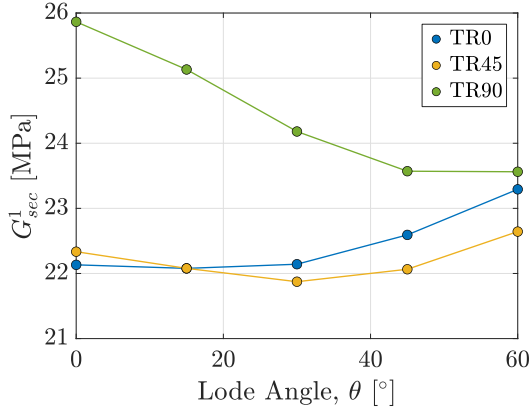


Figure 6. Variation of secant shear modulus during the first loading cycle for samples with different bedding plane orientations under various Lode angles.

To describe this relationship analytically, the following equation is identified as an effective approximation:

$$\frac{G_{sec}}{G_{sec}^1} = 30 \cdot \left(\exp \left(\frac{\varepsilon_q^{acc}}{\varepsilon_{q,ref}^{acc}} \right)^b \right)^c \quad (11)$$

Here, the constants b and c are functions of the Lode angle θ , as illustrated on the right-hand side of Figures 8–10. $\varepsilon_{q,ref}^{acc}$ presents the reference deviatoric strain for $\theta = 0^\circ$ at $G_{sec}/G_{sec}^1 = 0.3$. These correlations provide valuable insights into how the shear modulus degrades with increasing deviatoric strain and θ , offering an empirical equation for predicting the stiffness response of soils under complex loading conditions and varying initial anisotropy. This methodology serves as a critical step toward a more accurate modeling of soil behavior, particularly in scenarios involving multiaxial stress states, which are common in practical geotechnical applications.

Figure 7 presents approximated curves of the normalized shear modulus degradation relations with $G_{sec}/G_{sec}^1 =$

Table 3. Summary of coefficients a_i determined by fitting $G_{sec}/G_{sec}^1 = \sum_{i=0}^4 a_i N^i$.

θ in $^\circ$	TR	a_0	a_1	a_2	a_3	a_4
0→180	0	9471	86.9	-10.3	0.297	-0.0029
	45	9655	48.0	-6.7	0.175	-0.0015
	90	9501	51.7	-2.5	0.032	-0.0001
15→195	0	9688	42.2	-8.3	0.263	-0.0029
	45	9702	35.0	-7.1	0.215	-0.0022
	90	9625	46.8	-3.4	0.059	-0.00034
30→210	0	9535	89.5	-12.4	0.402	-0.0046
	45	9690	47.1	-8.5	0.258	-0.0026
	90	9562	49.1	-3.6	0.063	-0.00037
45→225	0	9675	63.6	-10.4	0.349	-0.0040
	45	9675	56.9	-8.3	0.238	-0.0021
	90	9573	56.8	-3.8	0.067	-0.00040
60→240	0	9449	107.7	-13.2	0.399	-0.0041
	45	9702	35.0	-7.1	0.215	-0.0022
	90	9625	46.8	-3.4	0.0591	-0.00034

$\sum_{i=0}^4 a_i N^i$, whereby the calibrated constants a_0 , a_1 , a_2 , a_3 and a_4 are summarized in Table 3. A fourth-order polynomial function with respect to the number of cycles can reproduce the observed behavior. These relations may be used as empirical equations to check either the performance of constitutive equations or for an initial estimation of the degradation rate of the secant shear modulus. In Figure 7, the observed behavior of the variation of secant shear modulus with the number of cycles highlights the influence of initial anisotropy. Notably, the figure demonstrates that as the bedding plane angle increases, the degradation of the secant shear modulus decreases. This correlation suggests that the initial anisotropy plays a significant role in mitigating the degradation of the secant shear modulus or the liquefaction resistance.

4.4. Excess pore water pressure and strain accumulation

Figure 11 illustrates the accumulation of deviatoric strain, ε_q^{acc} , as a function of the number of cycles, N , across various loading directions, θ , for samples with different initial fabric orientations. A similar trend is observed when compared to the development of shear modulus with the number of cycles. For TR0 and TR90 samples, the highest resistance to deformation is exhibited under a loading direction of $\theta = 0^\circ$, whereas for TR45, the greatest stiffness is achieved along loading paths with $\theta = 60^\circ$.

The generation of normalized excess pore water pressure as a function of the number of cycles, shown in Figure 12, follows the same trend as the $\varepsilon_q^{acc} - N$ and $G_{sec}/G_{sec}^1 - N$ curves. It is evident that the buildup of excess pore water pressure precedes and triggers the degradation of shear modulus, which subsequently leads to the accumulation of deformation.

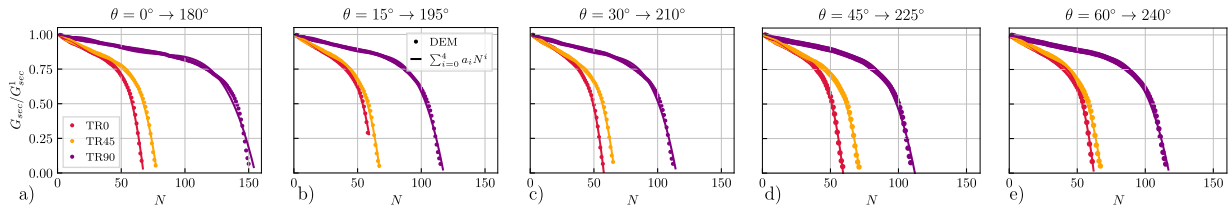


Figure 7. Approximation of secant shear modulus curve via $G_{\text{sec}}/G_{\text{sec}}^1 = \sum_{i=0}^4 a_i/N^i$. The dots represent the DEM results, while the solid lines depict the numerical approximations.

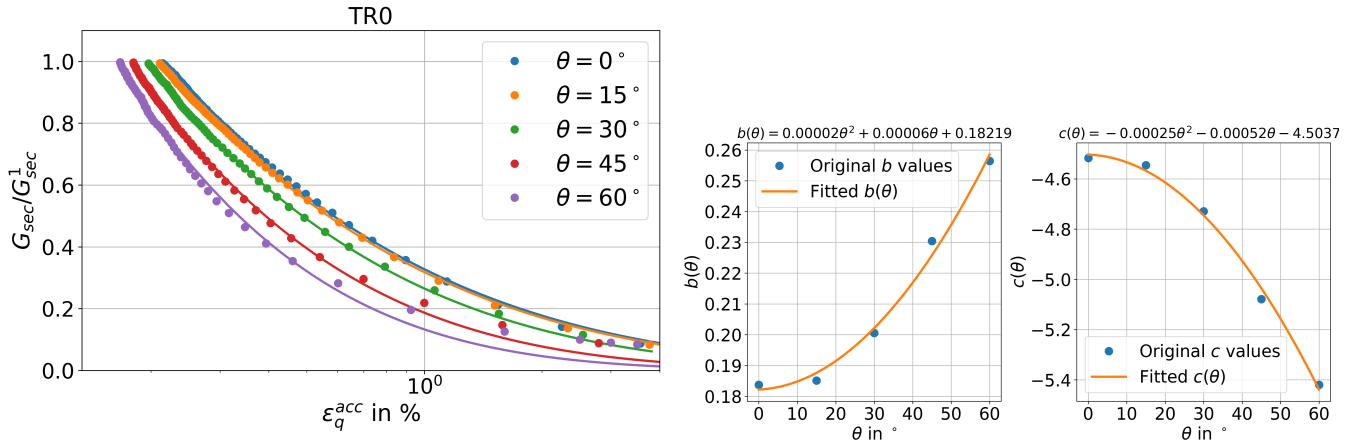


Figure 8. Approximation of secant shear modulus curve via $G_{\text{sec}}/G_{\text{sec}}^1 = 30 \cdot (\exp(\varepsilon_q^{\text{acc}})^b)^c$ for TR0. The dots represent the DEM results, while the solid lines depict the numerical approximations.

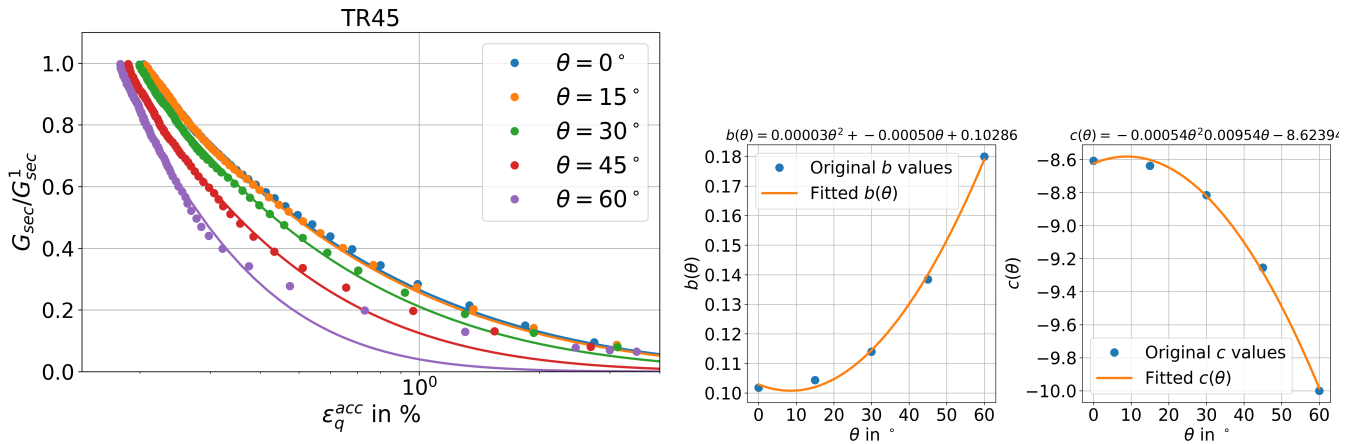


Figure 9. Approximation of secant shear modulus curve via $G_{\text{sec}}/G_{\text{sec}}^1 = 30 \cdot (\exp(\varepsilon_q^{\text{acc}})^b)^c$ for TR45. Circular markers denote the DEM simulations and the solid lines the approximation results.

5. Micro-scale observations

5.1. Fabric evolution of granular assemblies under cyclic shearing

In this section, variations in the diagonal components of the fabric tensor for TR0 samples with $e_0 = 0.589$ and $p'_0 = 100$ kPa are analyzed under continuous shearing. The results are illustrated in Figure 13. Each component of the fabric tensor reflects the intensity of inter-particle contacts in a certain direction. For example, F_z indicates the principal component of the fabric tensor in z-direction (vertical

direction as shown in Figure 1). The fabric of inter-particle contacts evolves as new contacts are formed, existing contacts are lost, and the orientations of contacts change. In this sense, changes in F_z reflect alterations in these three factors in the z direction. The same concept holds for F_x and F_y .

According to Figure 13(a), (b) & (c), the intensity of fabric tensor in the x, y and z directions, converges asymptotically to a maximum and minimum value in compression and extension sides, respectively. In the compression loading mode with $\theta = 0^\circ$, the maximum value of F_z exceeds the

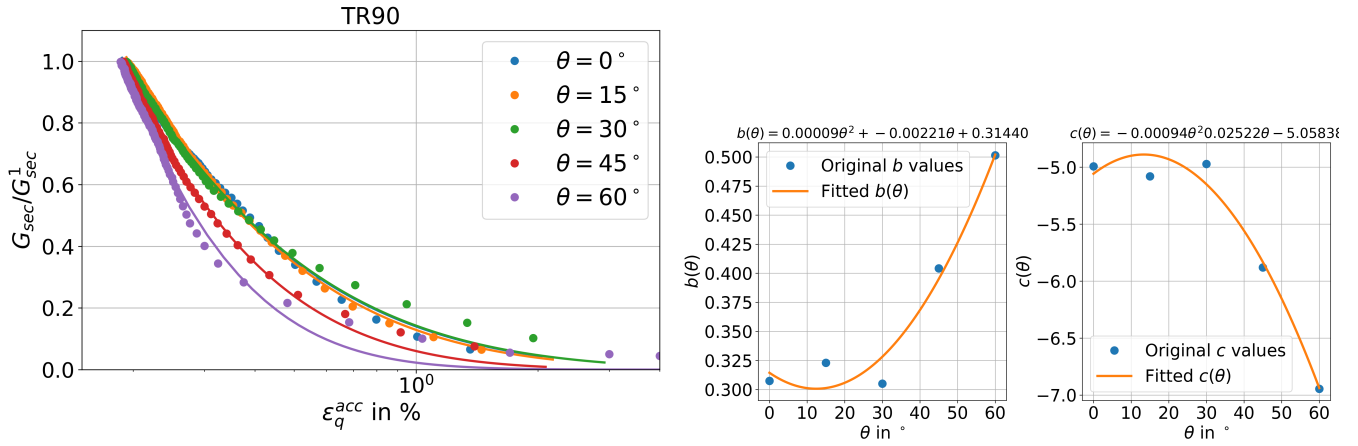


Figure 10. Approximation of secant shear modulus curve via $G_{sec}/G_{sec}^1 = 30 \cdot (\exp(\varepsilon_q^{acc})^b)^c$ for TR90. Circular markers denote the DEM simulations and the solid lines the approximation results.

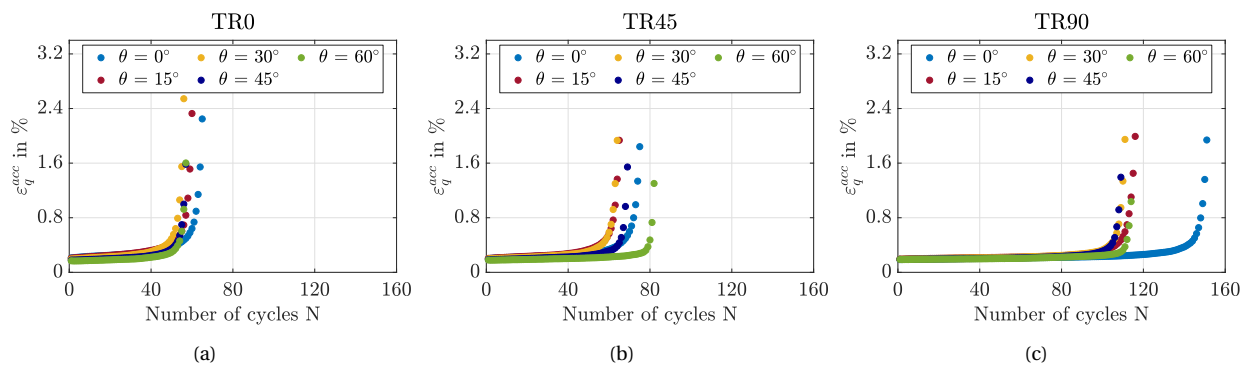


Figure 11. Variations of accumulated deviatoric strain ε_q^{acc} versus the number of cycles N for medium-dense granular assemblies: (a) TR0, (b) TR45 and (c) TR90.

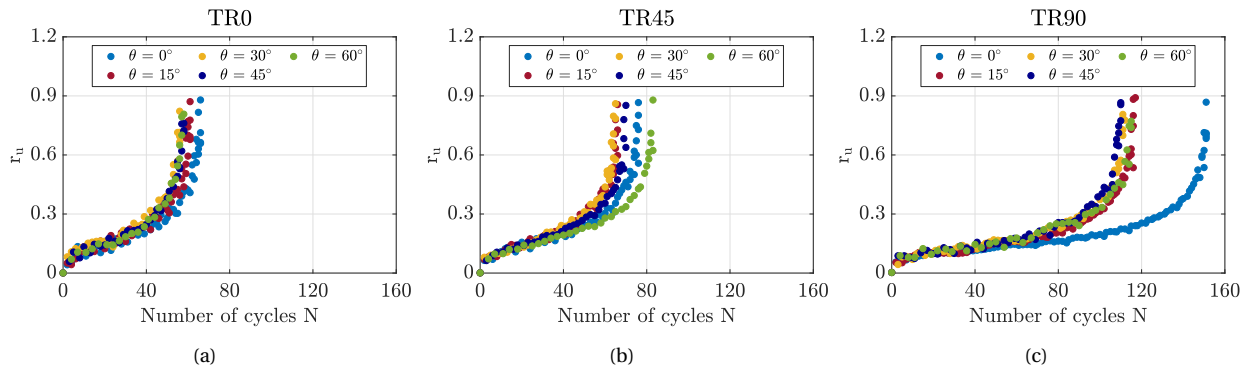


Figure 12. Variations of normalized excess pore water pressure r_u versus the number of cycles N for medium-dense granular assemblies: (a) TR0, (b) TR45 and (c) TR90.

maximum values of both F_x and F_y . It is important to highlight that under axisymmetric compression loading conditions with $\theta = 0^\circ$, the relationship $\sigma'_x = \sigma'_y < \sigma'_z$ holds true. In general, for $0^\circ \leq \theta \leq 60^\circ$, the major principal stress is applied in the vertical direction, i.e., the z -direction. As shown in Figure 13, for all values of θ , both the maximum and average value of fabric anisotropy in the z -direction, F_z , surpasses that in the x -direction, F_x , and y -direction, F_y . This

indicates that the fabric has been reoriented in favor of contact orientation along the major principal stress direction. X-ray tomography results, as visualized by Wiebicke et al. [2020] during conventional triaxial tests, also confirm significant anisotropy, mainly due to the preferential orientation of contact normals in the vertical direction.

Furthermore, a comparison of Figure 3 with Figure 13 reveals that, for each sample, the rate of changes in the

magnitudes of the stress ratios closely correlates with the variations in the diagonal components of the fabric tensor. For instance, after $\varepsilon_q = 3.4\%$, as shown in Figures 3(a) and Figures 13(a-c), both the rate of variation in stress ratio versus deviatoric strain and the fabric components versus deviatoric strain increases. Moreover, it is observed that the degree of fabric anisotropy is more pronounced on the compression side than on the extension side, highlighting the dependency of induced anisotropy on the loading direction. Under compression loading, the stress ratio is generally higher compared to the extension side at the same strain level (see Figure 3, except for samples with $\theta = 60^\circ$), which may allow for a more significant development of particle arrangement. Overall, the relationship between the anisotropic distribution of contact normals and the mobilized stress ratio in real sands has been emphasized by Oda [1972] and is supported by findings from 3D DEM simulations of Gao et al. [2014], which have been incorporated into the development of constitutive models Norouzi and Lashkari [2021].

Considering the last fourth of the cycle in Figures 13(a) and (b), where the deviatoric strain level decreases from $\varepsilon_q=3.4\%$ to $\varepsilon_q=1.7\%$, F_x and F_y decrease from 0.355 to 0.3. This decline suggests a reduction in contacts along the x and y loading directions. In contrast, F_z increases from 0.27 at $\varepsilon_q = 3.4\%$ to 0.4 at $\varepsilon_q = 1.7\%$, indicating the establishment of new contacts and changes in inter-particle interactions along the z direction. The greater increase in the rate of F_z compared to the reduction in F_x and F_y at the same strain level suggests that more contacts are being formed in z direction to compensate for the loss of contacts in both the x and y directions. It is noteworthy that for $\theta = 0^\circ$, the trends of F_x and F_y are very similar due to the axisymmetric boundary conditions and loading path. However, as θ increases to 60° , the amplitude of F_y decreases, resulting in an increase in the amplitude of F_x .

Under monotonic loading, it is recognized that the discrepancy between the loading direction and the direction of the contact-normal-based fabric tensor gradually diminishes as shearing progresses Li and Yu [2009], Wu et al. [2023], Wu and Yang [2023]. While the Lode angle is a scalar quantity derived from stress invariants, it has a geometric interpretation in the deviatoric (π) plane as the angle between the major principal stress direction and the loading path. The contact-normal fabric tensor, although formulated in Euclidean space, can also be projected onto the π -plane for comparison. Hence, the observed reduction in directional discrepancy between the loading direction and the fabric tensor during monotonic shearing is physically meaningful when viewed within this common projection framework. This conclusion is evident in the results presented in Figures 13, where increasing the Lode angle does not significantly affect the final values of the fabric components at the end of the shearing. In this sense, the fabric components converge to the same values at the end of the tests, regardless of the Lode angle. For example, for all Lode angle values $F_x \approx 0.3$, $F_y \approx 0.3$ and $F_z \approx 0.37$ are reached at the end of the tests which is close to the initial value of F_x , F_y and F_z . However, comparing Figures 13(a, d, g, j & m) reveals

that changes in the Lode angle impact the maximum value of F_x in both compression and extension loading modes. A similar qualitative trend is observed for F_y and F_z , where the maximum fabric anisotropy is influenced by changes in θ .

Figure 14 presents the variations in the fabric invariant, Δ , for TR0, TR45 and TR90 samples sheared with $e_0 = 0.589$, $p'_0 = 100$ kPa and $\theta = 0^\circ$. The initial fabric significantly influences the overall pattern of Δ variations versus deviatoric strain. Moreover, the maximum value of Δ on the compression side is reached at a lower strain level for TR0 compared to TR45 and TR90 samples. This trend is consistent with the stress ratio variations shown in Figures 3(a), (b), and (c), where the maximum stress ratio for TR0 samples is attained at a lower ε_q compared to TR45 and TR90 samples. Comparing Figure 3(a) with Figures 13(a-c) and Figure 14(a), it is evident that the changes in magnitudes of the stress ratios correspond closely to those of the diagonal components and invariant of the fabric tensor. For instance, F_x , F_y , and F_z vary alternatively between a maximum and minimum when the loading direction is reversed. The same trend is observed for the stress ratio in Figure 3(a). When $\eta > 0$, the value of fabric components continuously increases, while they decrease gradually when $\eta < 0$. In the context of three-dimensional DEM modeling of assemblies subjected to triaxial compression, Gao et al. [2014] analytically derived the correlation between stress and fabric tensor invariants. Oda [1972] also emphasized a distinct relationship between the anisotropic distribution of contact normals and the mobilized stress ratio in real sands. It is noteworthy that in both TR45 and TR90 samples, Δ reaches its maximum value at approximately $\varepsilon_q = 2.6\%$, suggesting a highly anisotropic internal structure before the onset of liquefaction. Furthermore, prior to liquefaction, Δ in TR45 and TR90 samples exhibit a decreasing evolution, whereas in TR0, it shows an increasing trend.

5.2. Variations in mechanical coordination number and redundancy index in granular assemblies under undrained cyclic shearing

Figures 15(a–c) depict the variation of the mechanical coordination number (MCN) versus deviatoric strain under undrained cyclic loading for the TR0, TR45, and TR90 specimens sheared with $e_0 = 0.589$, $p'_0 = 100$ kPa, and $\theta = 0^\circ$. As shown, the overall evolution of MCN is consistent across all three samples and qualitatively resembles the trend observed in the excess pore pressure evolution (Figure 4). Specimens with comparable initial void ratios show nearly identical MCN values at the onset of Shearing.

Granular assemblies can exhibit fluid-like behavior with negligible static shear modulus. The MCN, which accounts only for force-bearing contacts (i.e., excluding rattlers), is primarily influenced by particle shape, interparticle friction, and confining pressure Liu and Nagel [2010], O'Hern et al. [2002], van Hecke [2009], Yuan et al. [2019]. For assemblies composed of spherical particles, a *coordination number* of $CN = 4$ is typically considered a critical threshold separating

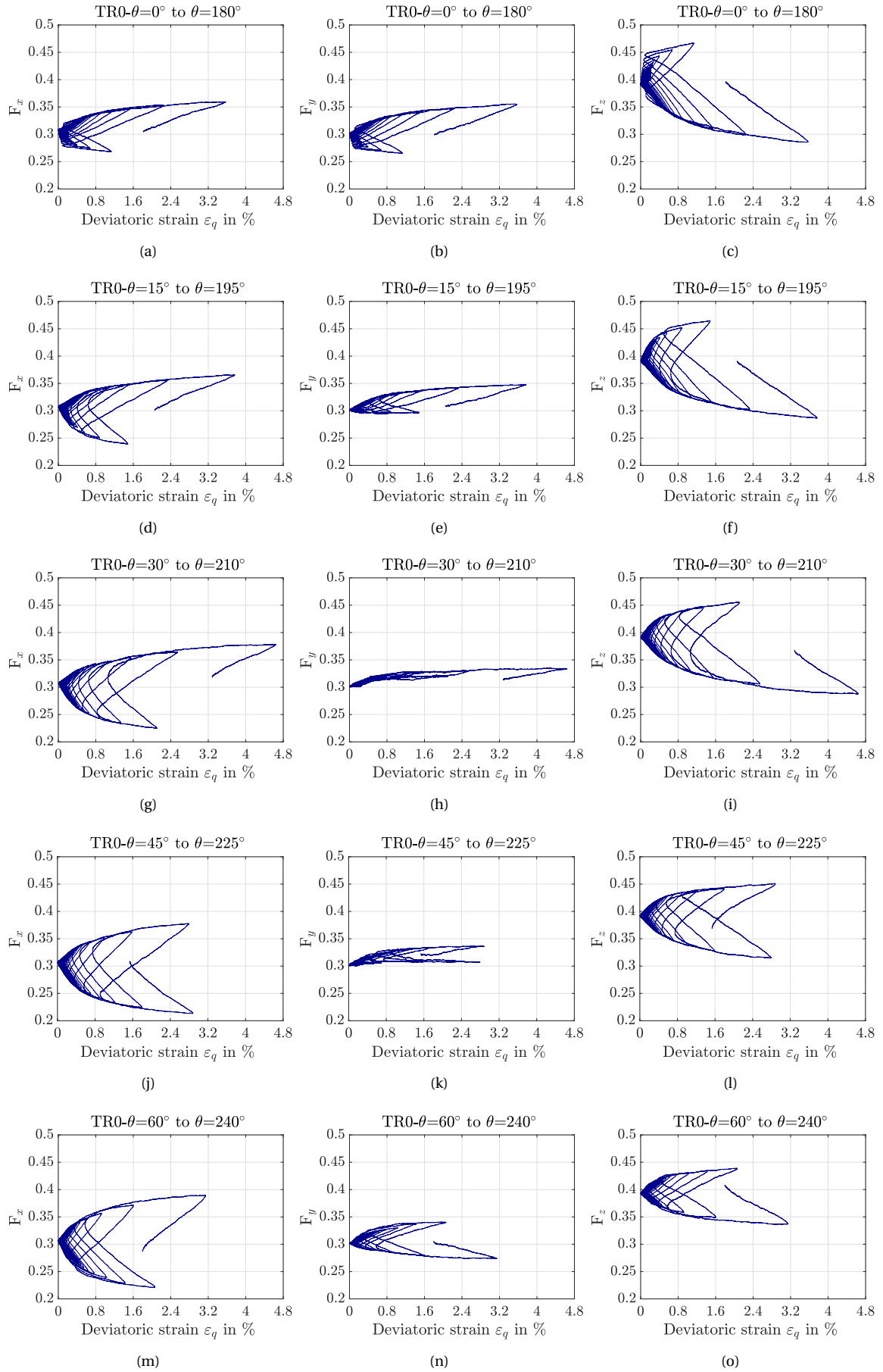


Figure 13. Variations of fabric components of TR0 assemblies with $e_0 = 0.589$, $p'_0 = 100$ kPa sheared under the undrained true triaxial condition with (a, b & c): $\theta = 0^\circ$ to $\theta = 180^\circ$; (d, e & f): $\theta = 15^\circ$ to $\theta = 195^\circ$; (g, h & i): $\theta = 30^\circ$ to $\theta = 210^\circ$; (j, k & l): $\theta = 45^\circ$ to $\theta = 225^\circ$ and (m, n & o): $\theta = 60^\circ$ to $\theta = 240^\circ$

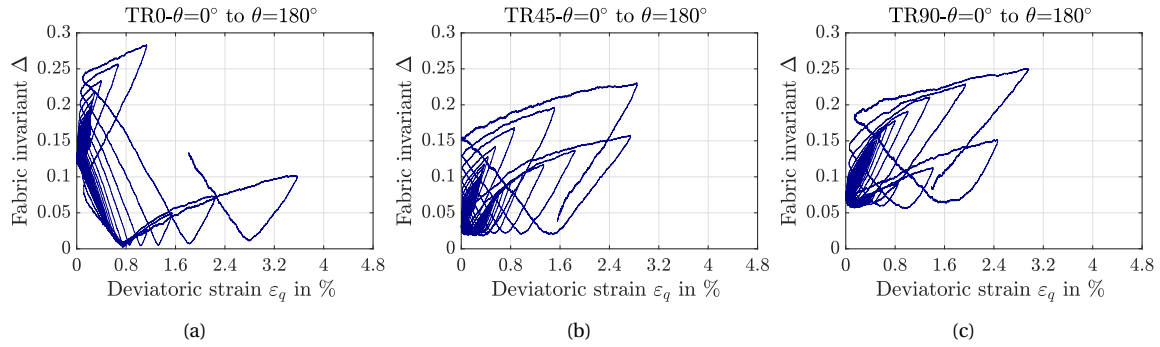


Figure 14. Variations of fabric invariants in semi-dense assemblies with $e_0 = 0.589$, $p'_0 = 100$ kPa sheared under the undrained true triaxial condition with $\theta = 0^\circ$, (a): TR0; (b): TR45 and (c): TR90

solid-like ($CN \geq 4$) and liquid-like ($CN < 4$) behavior Gong [2008], Gu et al. [2014]. When rattlers are excluded, the mechanical coordination number (MCN) provides a more refined measure of the load-bearing structure. Studies such as Yang et al. [2021] suggest that the onset of liquefaction in spherical assemblies is characterized by $MCN \approx 3.6$, while others report slightly lower thresholds—e.g., $MCN = 3$ Gu et al. [2020] and $MCN \approx 2.8$ Martin et al. [2020].

However, in this study, due to the use of clumped, non-spherical particles, higher MCN values are observed at the onset of instability. Specifically, $MCN \approx 4.5$ is reached across all assemblies during extension, which is considered indicative of the preliquefaction state. This is primarily due to shape-induced interlocking and enhanced contact stability, which delay the collapse of the contact network compared to spherical particles. Notable examples include studies on elliptical, concave, and polygonal particles, where coordination numbers remain above 4 under shear or dynamic conditions relevant to instability Basson et al. [2024], Ni et al. [2024], Salimi et al. [2025a,c].

A comparison of Figures 15(a–c) reveals that the TR0 specimen reaches $MCN \approx 4.5$ in fewer cycles compared to TR45 and TR90. This aligns with the macroscopic behavior discussed in Section 4, where a greater reduction in shear strength is observed in TR0 after approximately 60 cycles (see Figure 7). To further examine the evolution of the contact network, Figures 15(d–f) present the variation of the *redundancy index* I_R^f , which excludes floaters (particles with zero contacts). The redundancy index generally follows a similar trend to MCN, decreasing throughout the cyclic loading and converging toward unity, irrespective of initial fabric. These results are consistent with prior DEM studies Gong and Zha [2013], Martin et al. [2020], Zhang et al. [2023], Zhu et al. [2021], which associate the onset of liquefaction with a redundancy index approaching $I_R^f \approx 1$. Values of $I_R^f > 1$ indicate a solid-like, statically stable system, while $I_R^f < 1$ corresponds to a liquid-like, mechanically unstable state.

6. Summary and conclusion

In conclusion, this study explored the influence of anisotropy, both in initial fabric and induced by variations in applied

stress, on the stress-strain response of granular assemblies. The Discrete Element Method (DEM) combined with the Coupled Fluid Method (CFM) was utilized to simulate fluid-solid interactions under undrained conditions. Three transversely isotropic specimens, created using elongated particles, were analyzed, each with a unique initial fabric based on bedding plane angles of 0° , 45° , and 90° . Simulations were conducted under a constant total mean stress and a fixed Lode angle, providing insights into the anisotropic behavior of granular materials with varying Lode angles.

In general, the simulation results underscore the significant impact of initial fabric and Lode angle on the liquefaction susceptibility and maximum shear strength of granular assemblies. Notably, raising the bedding plane from 0° to 90° increases the number of cycles needed to reach liquefaction. This increase was primarily due to the alignment of the bedding plane with the direction of the major principal stress. The results suggest that the material fabric realigns in favor of contact orientation along the major principal stress direction. Furthermore, the Lode angle affects both the secant shear modulus and the rate of excess pore water pressure generation within the assemblies. A strong correlation was observed between the evolution of excess pore water pressure, the secant shear modulus, and the coordination number. Additionally, a qualitative correlation was identified between the evolution of fabric components and the stress ratio. These findings suggest that the behavior of granular assemblies can be comprehensively understood and predicted under varying loading conditions by analyzing the coordination number and the fabric orientations, specifically the components of the fabric tensor. The findings additionally suggest that while the Lode angle exerts an influence on the maximum stress ratio, it does not affect the mode of loading that ultimately leads to liquefaction.

Data availability

The datasets and materials used in this study are available from the corresponding author upon request.

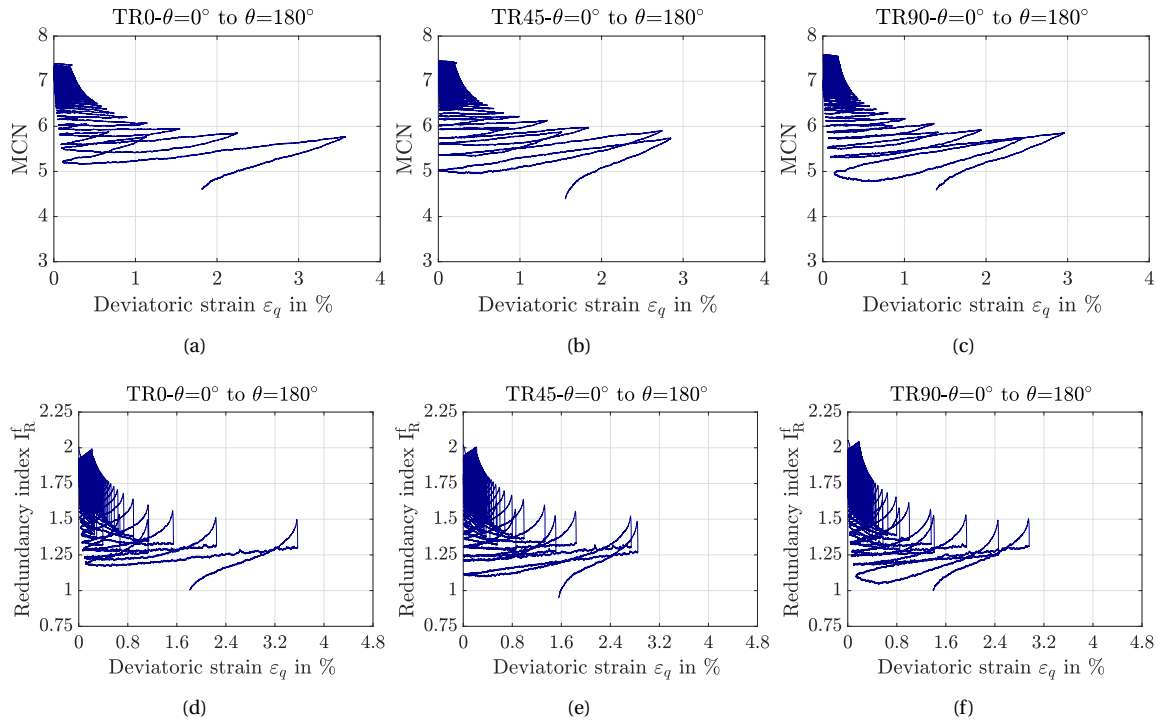


Figure 15. Variations of mechanical coordination number and redundancy index in semi-dense assemblies with $e_0 = 0.589$, $p'_0 = 100$ kPa sheared under the undrained true triaxial condition with $\theta = 0^\circ$, (a & d): TR0; (b & e): TR45 and (c & f): TR90

Declaration of competing interest

The authors have no relevant financial or non-financial interests to disclose. The complete review history is available online.

References

- Ajam Norouzi, M. and Seyedi Hosseininia, E. (2024). Effect of initial fabric anisotropy on cyclic liquefaction behavior of granular soils using discrete element method. *Granul. Matter*, 26(2):25.
- Basson, M. S., Martinez, A., and DeJong, J. T. (2024). Dem simulations of the liquefaction resistance and post-liquefaction strain accumulation of coarse-grained soils with varying gradations. *Comput. Geotech.*, 174.
- Boulanger, R. W. and Seed, R. B. (1995). Liquefaction of sand under bidirectional monotonic and cyclic loading. *J. Geotech. Eng.*, 121(12):870–878.
- Caous, D., Bois, C., Wahl, J.-C., Palin-Luc, T., and Valette, J. (2015). Analysis of multiaxial cyclic stress state in a wind turbine blade. In *20th international conference on composite materials (ICCM20), copenhagen, Denmark*.
- Christoffersen, J., Mehrabadi, M. M., and Nemat-Nasser, S. (1981). A micromechanical description of granular material behavior. *J. Appl. Mech.*, 48:339–344.
- Drescher, A. and De Jong, G. D. J. (2006). Photoelastic verification of a mechanical model for the flow of a granular material. In *Soil Mechanics and Transport in Porous Media: Selected Works of G. de Josselin de Jong*, pages 28–43. Springer.
- Gao, J., Sweetman, B., and Tang, S. (2022). Multiaxial fatigue assessment of floating offshore wind turbine blades operating on compliant floating platforms. *Ocean Eng.*, 261.
- Gao, Z., Zhao, J., Li, X.-S., and Dafalias, Y. F. (2014). A critical state sand plasticity model accounting for fabric evolution. *Int. J. Numer. Anal. Methods Geomech.*, 38(4):370–390.
- Gong, G. (2008). *DEM [Discrete Element Method] simulations of drained and undrained behaviour*. PhD thesis, University of Birmingham.
- Gong, G. and Zha, X. (2013). Dem simulation of undrained behaviour with preshearing history for saturated granular media. *Model. Simul. Mat. Sci. Eng.*, 21(2).
- González Tejada, I. and Antolin, P. (2022). Use of machine learning for unraveling hidden correlations between particle size distributions and the mechanical behavior of granular materials. *Acta Geot.*, 17(4):1443–1461.
- Gu, X., Huang, M., and Qian, J. (2014). Dem investigation on the evolution of microstructure in granular soils under shearing. *Granul. Matter*, 16(1):91–106.
- Gu, X., Zhang, J., and Huang, X. (2020). Dem analysis of monotonic and cyclic behaviors of sand based on critical state soil mechanics framework. *Comput. Geotech.*, 128.
- Guo, N. and Zhao, J. (2013). The signature of shear-induced anisotropy in granular media. *Comput. Geotech.*, 47:1–15.
- Hakuno, M. and Tarumi, Y. (1988). Sand liquefaction analysis by granular assembly simulation. In *Proceedings of ninth world conference on earthquake engineering*, volume 8, pages 231–236.

- Hamada, M. (1992). Large ground deformations and their effects on lifelines: 1964 Niigata earthquake. In *Case studies liquefaction and lifeline performance during past earthquakes: Japanese case studies*, pages 1–123.
- Holtz, R. D., Kovacs, W. D., and Sheahan, T. C. (1981). *An introduction to geotechnical engineering*, volume 733. Prentice-Hall Englewood Cliffs.
- Iai, S., Tobita, T., and Ozutsumi, O. (2013). Induced fabric under cyclic and rotational loads in a strain space multiple mechanism model for granular materials. *Int. J. Numer. Anal. Methods Geomech.*, 37(2):150–180.
- Irani, N., Salimi, M., Golestaneh, P., Tafili, M., Wichtmann, T., and Lederer, J. (2024). Deep learning-based analysis of true triaxial DEM simulations: Role of fabric and particle aspect ratio. *Comput. Geotech.*, 173.
- Ishihara, K. and Koga, Y. (1981). Case studies of liquefaction in the 1964 Niigata earthquake. *Soils Found.*, 21(3):35–52.
- Ishihara, K. and Yasuda, S. (1975). Sand liquefaction in hollow cylinder torsion under irregular excitation. *Soils Found.*, 15(1):45–59.
- Itasca, P. (2014). Version 5.0. *Itasca Consulting Group Inc. Minneapolis, United States*.
- Jiang, M., Zhang, A., and Li, T. (2019). Distinct element analysis of the microstructure evolution in granular soils under cyclic loading. *Granul. Matter*, 21:1–16.
- Ju, S.-H. and Mao, Y.-C. (2024). Research on offshore wind turbine support structures under seismic soil liquefaction. *Ocean Eng.*, 304.
- Khabazian, M. and Hosseininia, E. S. (2020). Instability of saturated granular materials in biaxial loading with polygonal particles using discrete element Method (DEM). *Powder Technol.*, 363:428–441.
- Knittel, L., Tafili, M., Tavera, C. G., and Triantafyllidis, T. (2023). New perspectives on preshearing history in granular soils. *Sci. Rep.*, 13(1):4576.
- Koseki, J., Matsuo, O., Ninomiya, Y., and Yoshida, T. (1997). Uplift of sewer manholes during the 1993 Kushiro-Oki earthquake. *Soils Found.*, 37(1):109–121.
- Lashkari, A., Khodadadi, M., Binesh, S. M., and Rahman, M. M. (2019). Instability of particulate assemblies under constant shear drained stress path: DEM approach. *Int. J. Geomech.*, 19(6).
- Li, X. and Yu, H.-S. (2009). Influence of loading direction on the behavior of anisotropic granular materials. *Int. J. Eng. Sci.*, 47(11-12):1284–1296.
- Li, X. S. and Dafalias, Y. F. (2012). Anisotropic critical state theory: role of fabric. *J. Eng. Mech.*, 138(3):263–275.
- Lin, G.-L., Lu, L.-Y., Lei, K.-T., Liu, K.-Y., Ko, Y.-Y., and Ju, S.-H. (2021). Experimental study on seismic vibration control of an offshore wind turbine with TMD considering soil liquefaction effect. *Mar. Struct.*, 77.
- Liu, A. J. and Nagel, S. R. (2010). The jamming transition and the marginally jammed solid. *Ann. Rev. Cond. Matter Phys.*, 1(1):347–369.
- Liu, G., Rong, G., Peng, J., and Zhou, C. (2015). Numerical simulation on undrained triaxial behavior of saturated soil by a fluid coupled-DEM model. *Eng. Geol.*, 193:256–266.
- Liu, X., Jia, Y., Zheng, J., Shan, H., and Li, H. (2013). Field and laboratory resistivity monitoring of sediment consolidation in China's Yellow River estuary. *Eng. Geol.*, 164:77–85.
- Lü, X., Zeng, S., Qian, J., and Huang, M. (2017). DEM analysis of the shear strength of cross-anisotropic sand with non-spherical particles. *Géotechnique Letters*, 7(3):230–236.
- Martin, E. L., Thornton, C., and Utili, S. (2020). Micromechanical investigation of liquefaction of granular media by cyclic 3D DEM tests. *Géotechnique*, 70(10):906–915.
- Mo, W., Wang, R., Zhang, J.-M., and Dafalias, Y. F. (2024). Quantification of fabric evolution in granular material under cyclic loading. *Int. J. Numer. Anal. Methods Geomech.*, 48(3):701–726.
- Nguyen, H. B. K., Rahman, M. M., and Fourie, A. B. (2021). How particle shape affects the critical state, triggering of instability and dilatancy of granular materials—results from a DEM study. *Géotechnique*, 71(9):749–764.
- Ni, X., Ma, J., and Zhang, F. (2024). Mechanism of the variation in axial strain of sand subjected to undrained cyclic triaxial loading explained by DEM with non-spherical particles. *Comput. Geotech.*, 165.
- Norouzi, N. and Lashkari, A. (2021). An anisotropic critical state plasticity model with stress ratio-dependent fabric tensor. *Iranian Journal of Science and Technology, Transactions of Civil Engineering*, 45:2577–2594.
- Oda, M. (1972). The mechanism of fabric changes during compressional deformation of sand. *Soils Found.*, 12(2):1–18.
- O'Hern, C. S., Langer, S. A., Liu, A. J., and Nagel, S. R. (2002). Random packings of frictionless particles. *Phys. Rev. Lett.*, 88(7).
- Okada, Y. and Ochiai, H. (2007). Coupling pore-water pressure with distinct element method and steady state strengths in numerical triaxial compression tests under undrained conditions. *Landslides*, 4(4):357–369.
- Petalas, A. L., Dafalias, Y. F., and Papadimitriou, A. G. (2020). Sanisand-F: Sand constitutive model with evolving fabric anisotropy. *Int. J. Solids Struct.*, 188:12–31.
- Pires-Sturm, A. P. and DeJong, J. T. (2022). Influence of Particle Size and Gradation on Liquefaction Potential and Dynamic Response. *J. Geot. Geoenv. Eng.*, 148(6).
- Radjai, F. and Dubois, F. (2011). *Discrete-element modeling of granular materials*. Wiley-Iste.
- Rodriguez-Arriaga, E. and Green, R. (2018). Assessment of the cyclic strain approach for evaluating liquefaction triggering. *Soil Dyn. Earthq. Eng.*, 113:202–214.
- Rondón, H., Wichtmann, T., Triantafyllidis, T., and Lizcano, A. (2009). Comparison of cyclic triaxial behavior of unbound granular material under constant and variable confining pressure. *J. Transp. Eng.*, 135(7):467–478.
- Salimi, M., Irani, N., Tafili, M., and Wichtmann, T. (2025a). The Effect of Lode Angle and Particle Aspect Ratio on Fabric Evolution in Granular Assemblies: A DEM-CFM Approach. In *IOP Conference Series: Earth and Environmental Science*, volume 1480. IOP Publishing.
- Salimi, M., Irani, N., and Wichtmann, T. (2025b). Dem-CFM analysis of Lode angle influence on the undrained cyclic behavior of anisotropically consolidated soils. *Sci. Rep.*,

- 15(1):1–18.
- Salimi, M. and Lashkari, A. (2020). Undrained true triaxial response of initially anisotropic particulate assemblies using CFM-DEM. *Comput. Geotech.*, 124.
- Salimi, M., Lashkari, A., and Tafili, M. (2024). Dem investigation on flow instability of particulate assemblies under coupling between volumetric and axial strains. *Acta Geot.*, pages 1–26.
- Salimi, M., Tafili, M., Irani, N., and Wichtmann, T. (2023a). Micro-mechanical response of transversely isotropic samples under cyclic loading. In *10th European Conference on Numerical Methods in Geotechnical Engineering (NUMGE2023)*, pages 1–6.
- Salimi, M., Tafili, M., Irani, N., and Wichtmann, T. (2023b). Micro-mechanical response of transversely isotropic samples under cyclic loading. In *10th European Conference on Numerical Methods in Geotechnical Engineering*.
- Salimi, M., Tafili, M., Irani, N., and Wichtmann, T. (2025c). Exploring Undrained Cyclic True Triaxial Behavior of Granular Assemblies Using DEM. In *IOP Conference Series: Earth and Environmental Science*, volume 1480. IOP Publishing.
- Salimi, M., Tafili, M., Prada-Sarmiento, L. F., Irani, N., Triantafyllidis, T., and Wichtmann, T. (2025d). Dem-CFM Analysis of Undrained Cyclic Behavior in Transversely Isotropic Granular Soils under True Triaxial Loading Paths. *J. Geot. Geoenv. Eng.*, 151(5).
- Tokimatsu, K., Tamura, S., Suzuki, H., and Katsumata, K. (2012). Building damage associated with geotechnical problems in the 2011 Tohoku Pacific Earthquake. *Soils Found.*, 52(5):956–974.
- van Hecke, M. (2009). Jamming of soft particles: geometry, mechanics, scaling and isostaticity. *J. Phys. Cond. Matt.*, 22(3).
- Wang, X., Zeng, X., Li, X., and Li, J. (2020). Liquefaction characteristics of offshore wind turbine with hybrid monopile foundation via centrifuge modelling. *Renewable Energy*, 145:2358–2372.
- Wei, J., Huang, D., and Wang, G. (2020). Fabric evolution of granular soils under multidirectional cyclic loading. *Acta Geot.*, 15:2529–2543.
- Wichtmann, T., Niemunis, A., and Triantafyllidis, T. (2007). Strain accumulation in sand due to cyclic loading: drained cyclic tests with triaxial extension. *Soil Dyn. Earthq. Eng.*, 27(1):42–48.
- Wichtmann, T., Niemunis, A., and Triantafyllidis, T. (2010). Strain accumulation in sand due to drained cyclic loading: on the effect of monotonic and cyclic preloading (Miner's rule). *Soil Dyn. Earthq. Eng.*, 30(8):736–745.
- Wichtmann, T. and Triantafyllidis, T. (2016). An experimental database for the development, calibration and verification of constitutive models for sand with focus to cyclic loading: part I—tests with monotonic loading and stress cycles. *Acta Geot.*, 11(4):739–761.
- Wiebicke, M., Andò, E., Viggiani, G., and Herle, I. (2020). Measuring the evolution of contact fabric in shear bands with X-ray tomography. *Acta Geot.*, 15(1):79–93.
- Wu, Q., Huang, L., Zhao, F., Qiu, Z., and Zheng, Y. (2023). Liquefaction behavior of inherently anisotropic sand under cyclic simple shear: Insights from three-dimensional DEM simulations. *Soil Dyn. Earthq. Eng.*, 171.
- Wu, Q. and Yang, Z. (2023). Unified discrete-element approach applying arbitrary undrained loading paths in element testing for granular soils. *Int. J. Numer. Anal. Methods Geomech.*, 47(1):3–22.
- Yang, M. and Taiebat, M. (2024). Exploring the role of fabric anisotropy in cyclic liquefaction resistance under non-hydrostatic consolidation: Insights from DEM analysis. In *E3S Web of Conferences*, volume 544. EDP Sciences.
- Yang, M., Taiebat, M., Mutabaruka, P., and Radjai, F. (2021). Evolution of granular materials under isochoric cyclic simple shearing. *Phys. Rev. E*, 103(3).
- Yang, Z. and Wu, Y. (2017). Critical state for anisotropic granular materials: a discrete element perspective. *Int. J. Geomech.*, 17(2).
- Yuan, Y., VanderWerf, K., Shattuck, M. D., and O'Hern, C. S. (2019). Jammed packings of 3D superellipsoids with tunable packing fraction, coordination number, and ordering. *Soft Matter*, 15(47):9751–9761.
- Zhang, A., Jiang, M., and Wang, D. (2023). Effect of fabric anisotropy on the cyclic liquefaction of sands: Insight from DEM simulations. *Comput. Geotech.*, 155.
- Zhao, C.-F., Pinzón, G., Wiebicke, M., Andò, E., Kruyt, N. P., and Viggiani, G. (2021). Evolution of fabric anisotropy of granular soils: X-ray tomography measurements and theoretical modelling. *Comput. Geotech.*, 133.
- Zhao, J., Zhu, Z., Zhang, D., Wang, H., and Li, X. (2024). Assessment of fabric characteristics with the development of sand liquefaction in cyclic triaxial tests: A DEM study. *Soil Dyn. Earthq. Eng.*, 176.
- Zhu, M., Gong, G., Xia, J., Liu, L., and Wilkinson, S. (2021). Effects of deviator strain histories on liquefaction of loose sand using DEM. *Comput. Geotech.*, 136.

Manuscript received 2nd September 2024, revised 5th May 2025 and 26th June 2025, accepted 26th June 2025.